Energy 79 (2015) 183–194

Contents lists available at ScienceDirect

Energy

journal homepage: www.elsevier.com/locate/energy

Influence of gamma irradiation exposure on the performance of supercapacitor electrodes made from oil palm empty fruit bunches

Najah Syahirah Mohd Nor [a], Mohamad Deraman [a,*], Ramli Omar [a], Awitdrus [b], Rakhmawati Farma [b], Nur Hamizah Basri [a], Besek Nurdiana Mohd Dolah [a], Nurul Fatin Mamat [a], Baharudin Yatim [a], Mohd Norizam Md Daud [c]

[a] School of Applied Physics, Faculty of Science and Technology, Universiti Kebangsaan Malaysia, 43600 Bangi, Selangor, Malaysia
[b] Department of Physics, Faculty of Mathematics and Natural Sciences, University of Riau, 28293 Pekanbaru, Riau, Indonesia
[c] Advanced Solar Cells Fabrication Laboratory, Solar Energy Research Institute, Universiti Kebangsaan Malaysia, 43600 Bangi, Selangor, Malaysia

ARTICLE INFO

Article history:
Received 25 April 2014
Received in revised form
21 October 2014
Accepted 2 November 2014
Available online 3 December 2014

Keywords:
Supercapacitor
Gamma irradiation
Carbon electrode
Specific power
Specific energy

ABSTRACT

Carbon-monolith electrodes for supercapacitors were prepared from GMs (green monoliths) made from pre-carbonized fibers of oil palm EFB (empty fruit bunches) and GMs of pre-carbonized EFB fibers exposed to gamma radiation at 5 kGy, 15 kGy, and 20 kGy. GMs and irradiated GMs were carbonized and activated to prepare ACM (activated-carbon-monolith) electrodes. The gamma radiation affected the pore structure of the ACM electrodes and the electrochemical performance of the supercapacitors; irradiation doses of 0 kGy, 5 kGy, 15 kGy and 20 kGy produced specific capacitances of 121 F g^{-1}, 196 F g^{-1}, 11 F g^{-1}, and 12 F g^{-1}, respectively. The irradiation dose of 5 kGy appears to be optimum and produces a specific power and specific energy of 236 W kg^{-1} and 5.45 W h kg^{-1}, respectively, representing 34% and 60% increases over ACM electrodes prepared from non-irradiated GMs.

1. Introduction

Supercapacitors, also known as EDLCs (electrochemical double-layer capacitors), operate in the energy range that lies between conventional capacitors and batteries. They have been widely used as an energy storage device that can store and release energy. Their delivery (charge–discharge) performance is better than commercial rechargeable batteries, and they also have a longer cycle life [1]. Supercapacitor applications as high power energy storage devices are mainly found in electronic and military devices, space flight technology, automotive and public transportation, and as low-power energy storage devices; they can be found in, for example, portable media players, game consoles, photographic flash, and printers [2]. Recently, supercapacitors have been critically analyzed for use in public transportation; specifically, they show promise in improving the performance of hybrid bus powertrain systems achieving both optimal size and good energy management [3].

The electrode is one of the major supercapacitor components. The other components are the electrolyte, current collector and separator. The energy storage process that occurs at the electrode–electrolyte interface involves the formation of an electric double layer via the migration of ionic charges in the electrolyte and electronic charges in the electrode. While many materials, such as graphene [4–7], CNTs (carbon nanotubes) [8,9], conducting polymers [10,11], triblock copolymers [12], metal oxides [13–16], carbon aerogels [17], activated carbons [18–21], and composites [22–24] have been widely developed as electrodes materials for supercapacitor, activated carbon is still the best porous electrode material for supercapacitors because of its high surface area, chemical stability, wide availability, and the simple and low cost preparation methods compared to other carbon-based materials, such as carbon nanotubes, carbon aerogels, and graphene. Significant effort has been dedicated to improving the properties of the activated carbon electrodes used in supercapacitors, such as studies on pore structure and surface chemistry because of the electrode's influence on the performance of supercapacitors [25,26].

Various methods, such as modifying the properties of the organic precursors or the pre-carbonized organic precursors used to produce carbon electrodes, have been applied prior to carbonizing the electrodes because the electrode properties, such as the pore structure and surface chemistry, are determined partly

* Corresponding author.
E-mail addresses: madra@ukm.edu.my, mderaman113@gmail.com (M. Deraman).

http://dx.doi.org/10.1016/j.energy.2014.11.002

by the properties of the precursors. This modification can be performed chemically using an activating agent, such as KOH [27], H_2SO_4 [28], H_3PO_4 [29], K_2CO_3 [30], or $ZnCl_2$ [31]; physically using a gas, such as CO_2 [32] or steam [33,34]; by a combination of physical and chemical methods [35–37]; or by microwave irradiation [38]. Additionally, this modification can be performed by mixing the organic precursor or pre-carbonized material with an additive, such as a metal oxide [39], conducting polymer [40], CNTs [41,42], graphene [43], graphene oxide [44], petroleum coke [45], or carbon fibers [46]. The purpose of these modifications is to improve the electrochemical performance of the supercapacitor. In the present study, a gamma irradiation technique is used to modify the properties of the pre-carbonized organic precursor, i.e., SACG (self-adhesive carbon grain) prepared from fibers from oil palm EFB (empty fruit bunches), which contain partially decomposed hemicellulose, cellulose and lignin. These macromolecules were sensitive to the γ-irradiation treatment [47–49], and the effect of the γ-irradiation was found to be strongly dependent on its dosage level. In the present study, the dosage applied to green monoliths of SACG was varied from 5 kGy to 20 kGy. The objective of the present study was to observe the effects of varying the γ-radiation dose on the properties of the carbon monolith electrodes produced from these green monoliths and correlate these effects with the performances of supercapacitors fabricated using these electrodes.

This paper is organized as follows: Section 2 presents the preparation and characterization procedures of electrodes from non-irradiated and γ-irradiated green monoliths of pre-carbonized oil palm fibers. Section 3 reports the results and discussion of physical and electrochemical data characterizing non-irradiated and γ-irradiated electrodes. Section 4 presents the conclusions of this study.

2. Materials and methods

2.1. Electrode preparation and cell fabrication

EFB fibers were supplied by Sabutek Sdn. Bhd. SACGs with an average particle size less than 106 μm were prepared from EFB fibers by pre-carbonization (Furnace CTMSB46), milling for 36 h (ball mill AC Motor BS 500-110) and sieving (Matest 24030 Brembate Sopra (BG)) [50]. A 30 g sample of SACG powder was poured into 300 ml of boiling water, stirred for 1 h, and dried in an oven at 100 °C for 48 h. Approximately 10 g of the dried mixture was milled for 20 min to obtain a homogeneous SACG powder. Following this step, 0.75 g of the mixture was placed inside a mold with a diameter of 20 mm and converted into GMs (green monoliths) using a press pelletizing machine (VISITEC 2009-Malaysia).

The GMs were sent for γ-irradiation treatment at dosages of 5, 15, and 20 kGy to produce the irradiated samples GM-5, GM-15 and GM-20, respectively, using a ^{60}Co γ-irradiation source (Gammacell 220 Excel). The non-irradiated and irradiated GMs were carbonized in a carbonization furnace (Vulcan Box Furnace 3-1750) under a 1.5 L min^{-1} flow of N_2 gas, at 800 °C using our previous multi-step heating profile [51] to produce CMs (carbon monoliths). These carbon monoliths were activated using CO_2 (1.0 L min^{-1}) at 800 °C with a multi-step heating profile [45,52,53] for 3 h at a heating rate of 5 °C min^{-1} to produce ACMs (activated carbon monoliths), labeled ACM-0, ACM-5, ACM-15 and ACM-20, respectively. After being polished to a thickness of 0.4 mm, the polished ACM-0 and other ACMs were used as electrodes in symmetrical supercapacitor cells using 316 L stainless steel (0.02 mm thick) as the current collector, 1 M H_2SO_4 as the electrolyte and a Celgard separator

2.2. Physical characterizations

The dimensions (Mitutoyo 193-253) and masses (Mettler Toledo AB204) of the monoliths were measured to determine the density of the GMs, CMs and ACMs. Fourier Transform Infrared Spectroscopy (FTIR, Perkin Elmer Spectrum 400 FT-IR) was used to study the chemical structures of the ACMs. A field emission scanning electron microscope (FESEM, Zeiss SUPRA 55 VP) was used to study the microstructures of the ACMs. An X-ray diffractometer (Bruker AXS: model D8 Advance, wavelength of 1.5406 Å for CuK_α line from Copper X-ray sources) was used to record the XRD (X-ray diffraction) patterns of the ACMs. The liquid nitrogen (77 K) adsorption–desorption isotherm experiments were conducted to characterize the porosity of the ACMs using an instrument (Micromeretic ASAP 2010) equipped with software that can calculate the pore structure parameters of the samples, i.e., the BET surface area (S_{BET}), micropore surface area (S_{micro}), mesopore surface area (S_{meso}), micropore volume (V_{micro}), mesopore volume (V_{meso}) and average pore diameter (D). Raman spectra were recorded over a 200 cm^{-1} to 3200 cm^{-1} Raman shift range from the ACMs using a Renishaw inVia Raman Microscope (Raman microscope enclosure RE 04) employing a 514 nm laser beam.

2.3. Electrochemical characterization

The performances of the supercapacitor cells with ACMs as their electrodes were studied using EIS (electrochemical impedance spectroscopy), CV (cyclic voltammetry) and GCD (galvanostatic charge–discharge) methods on an electrochemical instrument-interface (Solartron SI 1286 and Solartron 1255HF Frequency Response Analyzer). All of the measurements were carried out at room temperature (25 °C).

Using the EIS data, the C_{sp} of the electrodes was determined using equation (1):

$$C_{sp} = -\frac{1}{\pi f_l Z_l'' m} \tag{1}$$

where f_l is the lowest frequency, Z_l'' is the imaginary impedance at f_l and m is the weight of electrode. The EIS data as functions of the frequency were analyzed using equations (2)–(4):

$$C(\omega) = C'(\omega) - jC''(\omega) \tag{2}$$

$$C''(\omega) = Z'(\omega) \Big/ \omega |Z(\omega)|^2 \tag{3}$$

$$C'(\omega) = -Z''(\omega) \Big/ \omega |Z(\omega)|^2 \tag{4}$$

where $Z(\omega)$ is equal to $1/j\omega C(\omega)$, $C'(\omega)$ is the real capacitance, $C''(\omega)$ is the imaginary capacitance, $Z'(\omega)$ is the real impedance and $Z''(\omega)$ is the imaginary impedance [54].

From the voltammograms, the C_{sp} of the electrodes was determined using equation (5):

$$C_{sp} = \frac{2i}{Sm} \tag{5}$$

where i is the electric current, S is the scan rate and m is the weight of electrode.

From the GCD data (charge–discharge curve) recorded at a selected current density, the C_{sp} of the electrode was determined using equation (6):

$$C_{sp} = \frac{2i}{\left(\frac{\Delta V}{\Delta t}\right)m} \quad (6)$$

where i is the discharge current, ΔV is the voltage and Δt is the discharge time [55–57]. The values of the specific power (P) and specific energy (E) were also calculated from the GCD data using equations (7) and (8), respectively:

$$P = \frac{Vi}{m} \quad (7)$$

$$E = \frac{Vit}{m} \quad (8)$$

where i is the discharge current, V is the voltage (excluding the iR drop occurring at the beginning of the discharge) and t is time [58].

3. Results and discussion

3.1. FTIR analysis

The FTIR spectra in the range of wavenumbers from 400 to 4000 cm^{-1} for GM and γ-irradiated GM samples are shown in Fig. 1. The patterns of prominent peaks or bands in Fig. 1 for non-irradiated GMs are typical for lignocellulosic materials and are similar to those in the FTIR spectra reported for EFB [59,60], dried date pits [61] and jute fibers [62]. Assignments of these bands to their corresponding functional groups were reported in Refs. [63–65] for EFB samples, and in general, the bands involved C–O and C–H bonds in the macromolecules found in the EFB. Some differences between the FTIR spectra of the non-irradiated GMs and the precursors in Refs. [63–65] can be detected because the GMs were prepared from pre-carbonized EFB whose hemicellulose was almost fully decomposed, and the lignin and cellulose were partially decomposed during pre-carbonization. Comparison of the FTIR spectra of GM-0 and GM-5 shows that irradiation at 5 kGy can slightly change some of the band intensities, shapes and positions, and also produce new bands. Based on the GM-15 and GM-20 spectra, further increases in the dosage may cause further changes in the spectra. A band at ~2160 cm^{-1} was found to be unaffected by the irradiation. This band is associated with C≡C (alkynes) and triple bonds, which are not easily broken by the energy of the irradiation used here [66]. Despite these unchanged bands, the other spectral changes shown in Fig. 1 (GM-0–GM-20) are strong evidence that irradiation above 5 kGy can significantly alter the lignocellulosic structure in the GMs, which means that the already weak chemical links between the macromolecules in the GMs, due to pre-carbonization, were further weakened by the irradiation.

3.2. Physical characterization results

Fig. 2 compares the XRD data of all of the ACMs from the non-irradiated and irradiated GMs. These data show that all of the ACMs have a turbostratic structure, which implies that the building blocks of the ACMs are composed of graphitic-like microcrystallites that are randomly oriented and distributed throughout the samples [45,67,68]. All of the ACMs shows a similar diffraction pattern with two broad peaks at diffraction angles of 25° and 41.6°, corresponding to the (002) and (100) peaks, respectively. From these broad peaks, the values of the structural parameters, such as the interlayer spacing, (d_{002} and d_{100}) and microcrystallite dimensions [L_c (stack height) and L_a (stack width)], were determined. The values of d_{002} and d_{100} were calculated using Bragg's equation: $n\lambda = 2d\sin\theta$, where $n = 1$, λ is the wavelength (1.5406 Å) of the X-ray radiation and θ is the Bragg angle representing the position of the (002) and (100) diffraction peaks. The values of L_c, determined from the (002) peak, and L_a, determined from the (100) peak, were calculated using the Debye–Scherrer equation: $L_{c,a} = K\lambda/\beta_{c,a}\cos\theta$, where K is the shape factor equal to 0.89 and 1.84 for L_c and L_a, respectively, and $\beta_{c,a}$ is the full width at half maximum of the symmetrically shaped diffraction peaks.

The calculated values of the structural parameters are shown in Table 1. Small changes in the d_{002} and d_{001} values do not indicate a systematic trend that can be correlated with the change in dosage. However, the microcrystallite dimensions (L_c and L_a) in the ACMs seem to change significantly with the dosage. These results could be further analyzed in terms of the ratios of L_c/d_{002} and L_c/L_a. The former ratio represents the mean number of planes in the microcrystallites (N_p), while the latter ratio represents the relative density of edge and basal planes in the microcrystallites. The relative density of edge and basal planes is a measure of the edge orientation of the microcrystallites. The values of N_p (L_c/d_{002}) in Table 1 clearly indicate that increasing the dosage up to 5 kGy causes the microcrystallites in the ACMs to have higher N_p values, and above this dosage level, the N_p values begin to decrease with increasing dosage. The values of the latter ratio seem to increase significantly for 5 kGy dosage and started to decrease as the dosage increased. The values of this ratio for carbon samples produced under other experimental conditions using a coffee endocarp precursor [69] for

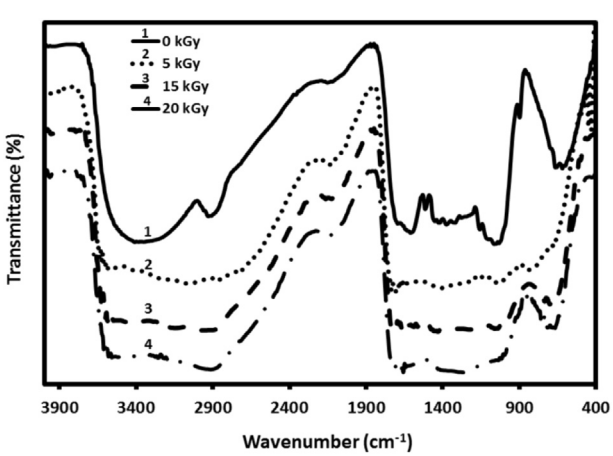

Fig. 1. FTIR spectra for non-irradiated and γ-irradiated GMs at different γ-radiation

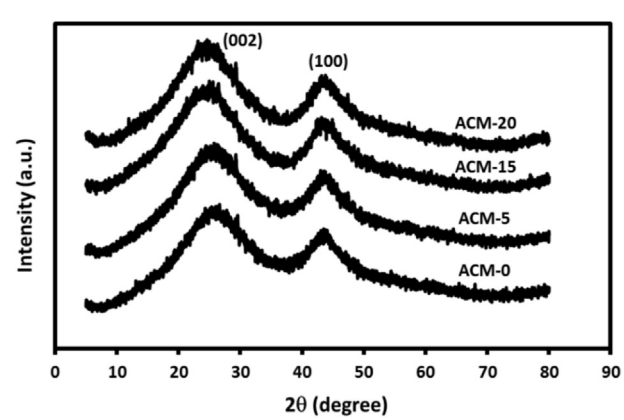

Fig. 2. XRD pattern for the ACMs from non-irradiated and γ-irradiated GMs at different γ-radiation dosage.

Table 1
Interlayer spacing, crystallite dimension, and ratios of L_c/L_a and L_c/d_{002} for all ACMs.

ACMs	d_{002} (Å)	d_{100} (Å)	L_c (Å)	L_a (Å)	L_c/L_a	L_c/d_{002}
ACM-0	3.574	2.057	11.183	48.465	0.230	3.128
ACM-5	3.639	2.054	13.078	46.383	0.281	3.593
ACM-15	3.667	2.049	11.357	55.044	0.206	3.097
ACM-20	3.635	2.050	10.677	57.188	0.186	2.937

the supercapacitor electrodes have been reported to be within the range of 0.32–0.67, and a carbon-based electrode produced using the same experimental conditions, excluding the γ-radiation exposure, and oil palm empty fruit bunches [53] reported values for the latter ratio between 0.22 and 0.74, which are similar to the L_c/L_a values listed in Table 1.

3.3. FESEM micrographs

FESEM micrographs of the fractured surface of ACM-0, ACM-5, ACM-15 and ACM-20 samples recorded at low magnification (1.00 K ×) are shown in Fig. 3(a)–(d), respectively. All of the micrographs, which show the rough surfaces of the grains, rough grain boundaries and smooth surfaces, indicate the porous characteristics of the samples made of microstructures with a network of open pores. The microstructure shown in Fig. 3(a) is nearly the same as those in Fig. 3(b)–(d), indicating that the γ-irradiation applied to the green monolith did not lead to the changes in the ACM (and activated to prepare activated-carbon-monolith) microstructure on this scale. FESEM micrographs of the fractured surfaces of all of the samples recorded at higher magnification (15 K x) are shown in Fig. 4(a)–(d), respectively. These high magnification micrographs show the microporous microstructure of the ACMs with open pores network distributed evenly throughout the samples. The effects of γ-irradiation are still not visible in these micrographs at this scale as all of them look nearly identical. It is possible that the differences between the micrograph shown in Fig. 4(a) and the others could only be observed in micrographs produced at much higher magnifications, which is beyond ability of the instrument used.

3.4. N_2 adsorption/desorption isotherms characterization

The N_2 adsorption/desorption isotherms for all ACMs prepared in this work are shown in Fig. 5 and have shapes that are typical for activated carbon samples [70,71]. All plots exhibit a very similar shape, and this shape has the characteristics of both type I and type IV isotherms as defined by the IUPAC classification scheme [72,73]. These types of isotherm curves indicate that all of the ACMs are porous samples consisting of micropores and mesopores. Although all of the plots show a similar shape or pattern, noticeable differences in their 'knee' shapes, hysteresis loops and levels of adsorption could be observed. These behaviors result from the different doses of γ radiation applied to the GMs. Quantitatively, these effects could be represented in terms of the values of the pore structure parameters shown in Table 2. The results in this table clearly show that excessive irradiation dosages applied to GMs can cause the ACMs to experience significant losses in their surface areas and porosities. The ACM-5 sample seems to have the largest volume and surface area contributions from mesopores, which are needed to transport electrolyte ions into the micropores during charging and discharging.

3.5. Raman spectroscopy

Fig. 6 shows the Raman spectra of the ACMs, revealing that all exhibited two sharp bands in the 1100–1800 cm^{-1} region and a broad band in the 2400–3200 cm^{-1} region; these are typical bands for the activated carbon [74]. The band intensity of the ACMs from irradiated GMs was less than that of non-irradiated GMs. Note that, for structurally higher ordered graphite, only one band appeared, in the 1100–1700 cm^{-1} region. The D band at ~1350 cm^{-1} represents disordered carbon, and the G band at ~1580 cm^{-1} represents ordered (graphitic) carbon [75]. The degree of ordering or disordering in the samples is represented by the ratio of the intensities of the D

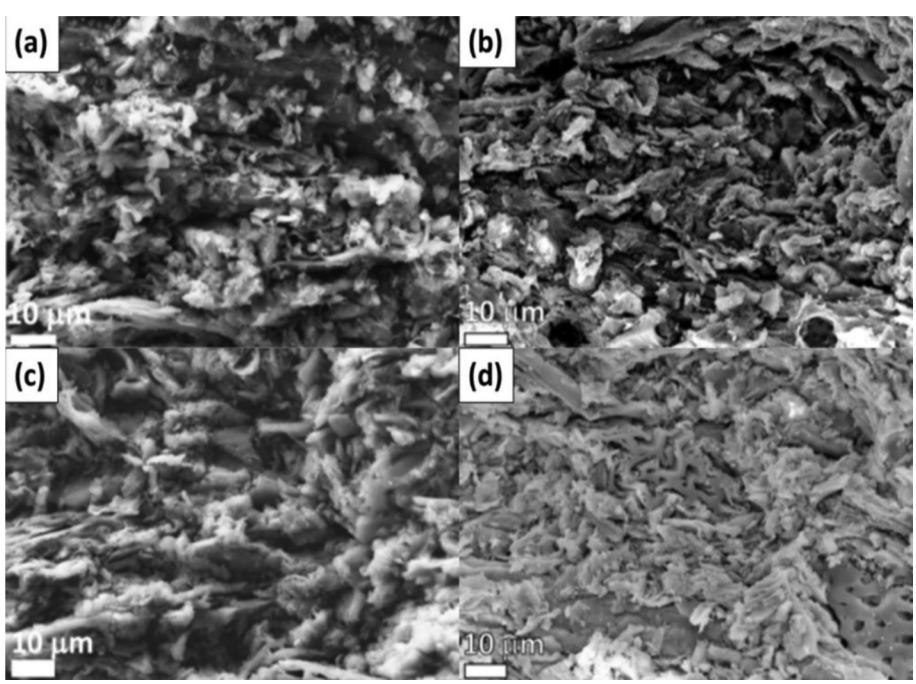

CM-15 and (d) ACM-20 at low magnification (1.00 K ×).

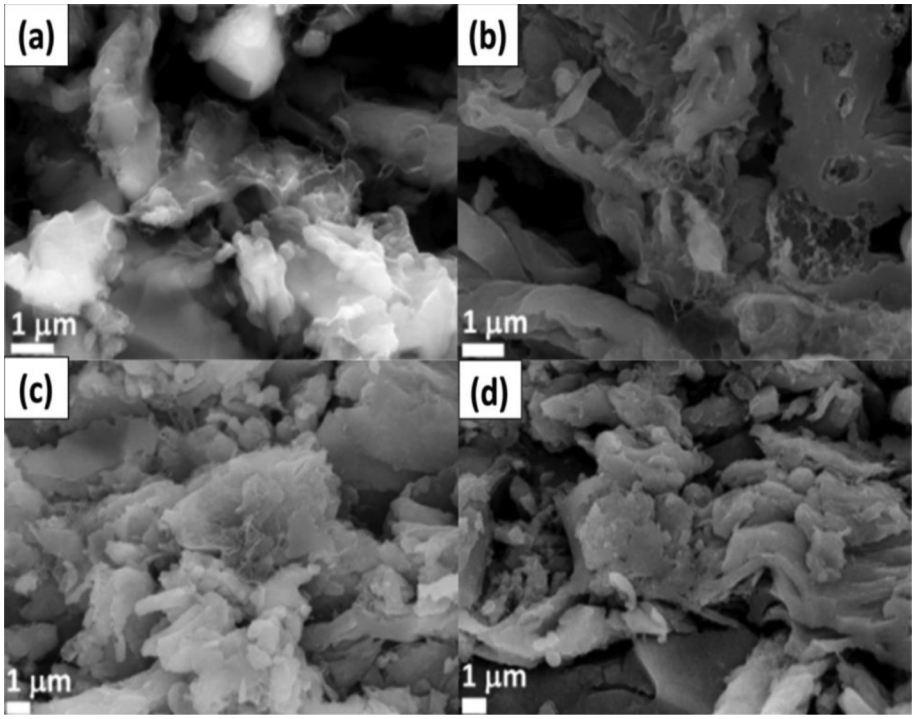

Fig. 4. FESEM micrographs for (a) ACM-0, (b) ACM-5, (c) ACM-15 and (d) ACM-20 at higher magnification (15 K ×).

band and G bands (I_D/I_G). The calculated I_D/I_G values from Fig. 6 were 0.925, 0.934, 0.933, and 0.917 for ACM-0, ACM-5, ACM-15, and ACM-20, respectively. These results indicate that an appropriate irradiation dosage applied to the GMs induces the greatest disordering in the electrodes, as shown by the highest I_D/I_G ratio for the ACM-5 electrode.

3.6. Electrochemical properties

3.6.1. Electrochemical impedance spectroscopy

The EIS data were recorded as Nyquist plots over the frequency range of 10^{-1} to 10^{6} Hz for the ACM-based supercapacitor cells, and these plots are shown in Fig. 7(a). The effects of the dosage on the small semicircle (first segment), Warburg diffusion line (second segment) and capacitive line (third segment) can be clearly observed in Fig. 7(a). In the high frequency region, there is a small semicircle that represents the dominant resistive nature of the supercapacitor consisting of an electrode/electrolyte/current-collector system. The left-intercept of the semicircle (Z″ value on the Z′ axis) represents the resistance (R_s) of the electrolyte in

Table 2
Pore characteristic parameter values for ACMs from non-irradiated and γ-irradiated GMs.

ACMs	ACM-0	ACM-5	ACM-15	ACM-20
S_{BET} ($m^2\ g^{-1}$)	802	768	552	615
S_{meso} ($m^2\ g^{-1}$)	108	163	68	83
S_{micro} ($m^2\ g^{-1}$)	694	605	484	583
V_{meso} ($cm^3\ g^{-1}$)	0.066	0.081	0.061	0.063
V_{micro} ($cm^3\ g^{-1}$)	0.325	0.286	0.228	0.274
D_p (nm)	1.986	1.989	2.066	2.027

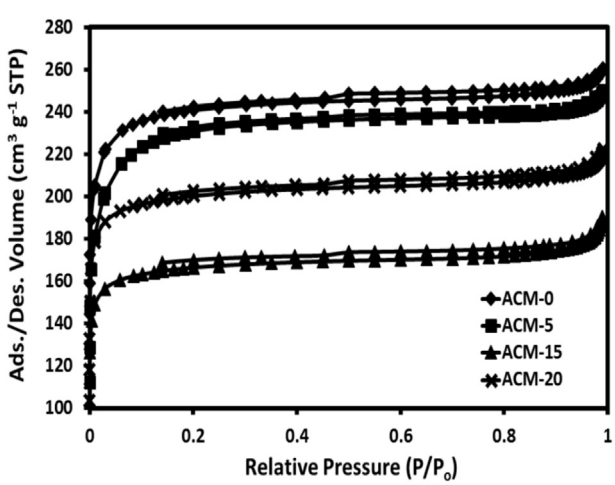

Fig. 5. Nitrogen adsorption–desorption isotherms for ACMs from non-irradiated and

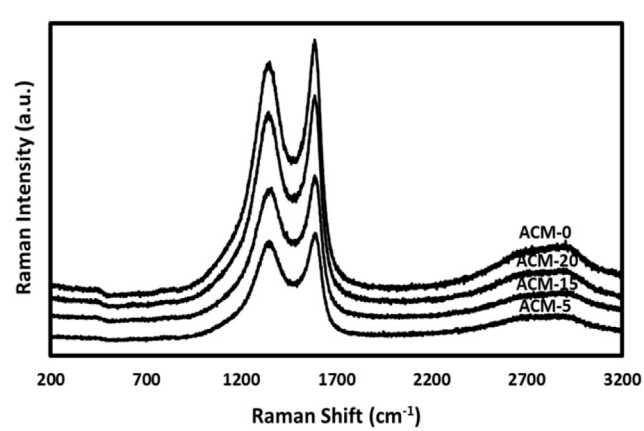

Fig. 6. Raman spectra for ACMs from non-irradiated and γ-irradiated GMs at different gamma radiation dosage.

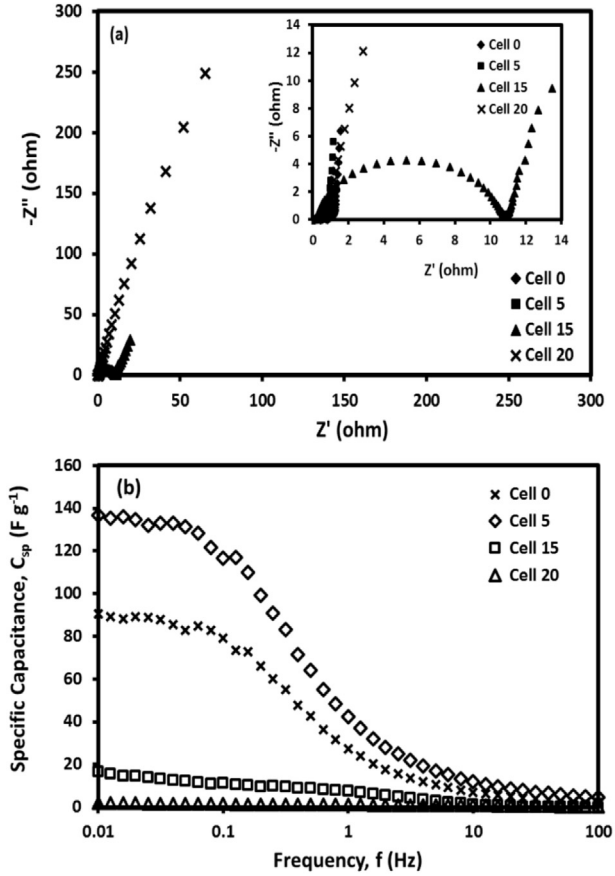

Fig. 7. (a) Nyquist plot and (b) Specific capacitance vs. frequency for all cell.

contact with the current collector and electrode. The right-intercept of the semicircle (Z″ value at the Z′ axis) represents the internal resistance (R_p) of the electrode. The ESR (equivalent series resistance) value is given by the diameter of the semicircle (R_p–R_s). The values of R_s, R_p and ESR for the cells obtained from the plot in Fig. 7(a) are listed in Table 3. These results indicate no specific dependency of ESR on the dosage. A similar trend appeared in the resistance or resistivity of electrodes determined by a four-point probe technique; these data were 0.275 Ω (or 11.7 Ω cm), 0.492 Ω (or 19.8 Ω cm), 0.308 Ω (or 12.4 Ω cm), and 0.217 Ω (or 8.73 Ω cm) for ACM-0, ACM-5, ACM-15, and ACM-20, respectively. The magnitudes of these ESR and resistance values are near the typical range of ESR values for carbon-based supercapacitors. For example, Kim et al. (2006) have reported ESR values of 0.134–1.149 Ω for bamboo-based activated carbon electrodes [76]. Porous carbon microspheres derived from porous starch had ESR values of 0.17–0.2 Ω, as reported by Du et al. (2013) [77]. Deng et al. (2013) reported ESR values of 0.31–0.38 Ω using multiwalled carbon nanotube/cellulose composite nanofibers [42]. ESR values from 0.31 to 0.40 Ω have been obtained from carbon-nanotube-seaweed-based electrodes reported by Raymundo et al., 2011 [78].

Table 3
The values of R_s, R_p, ESR (EIS), f_o, and τ_o for all cells.

Cell	R_s (Ω)	R_p (Ω)	ESR (Ω) (EIS)	f_o (Hz)	τ_o (s)
ACM-0	0.298	0.806	0.507	0.050	19.952
ACM-5	0.350	0.523	0.173	0.063	15.848
ACM-15	0.199	10.772	10.572	0.020	50.125
ACM-20	0.269	0.372	0.102	7.943	0.126

In the middle frequency region, the second segment (straight line with a slope of approximately 45°) represents the combination of resistive and capacitive behaviors of the ions penetrating into the electrode pores. The length, slope and position of this segment appear to change with the dosage. A steep slope was found in carbon electrodes that efficiently permit ions to penetrate their pores [79].

In the low-frequency region, the third segment (straight, sharply increasing lines) represents dominance of capacitive behavior that results from the formation of the electric double layer system at the electrolyte/electrode interface; in this region, the ions can more easily diffuse into the micropores [79–82]. The third segment line begins at the knee frequency (f_o), and its corresponding resistance (R_k) is given by Z'_k. The f_o values are given in Table 3. These results indicate that the dosage may shift the capacitive regions of the cells to lower or higher resistive ranges. This straight line is shorter for ACM-5, and it leans more towards the vertical Z″ axis than the other three cells, indicating that the ACM-5 cell has better capacitive performance. The values of C_{sp} for all cells, calculated from the EIS data using equation (1), are shown in Table 4 and reveal that the ACM-5 cell has the highest C_{sp}. In Fig. 7(b), the C_{sp} calculated using equation (1) strongly depends on the frequency in the frequency region below 1 Hz, particularly for the ACM-5 cell, which shows a higher C_{sp} throughout the entire frequency region.

Fig. 8(a)–(d) show the Bode plot for the imaginary (Z″) and real (Z′) resistive portions of the ACM cells calculated using equations (3) and (4) as functions of the frequency. The Z′ and Z″ intercepts in Fig. 8 give the peak frequency value (f_o), which is associated with the relaxation time constant, τ_o, which defines the boundary between the regions of capacitive and resistive behaviors for the supercapacitor. It is well known that higher power delivery requires lower values of τ_o [83].

Based on the f_o values in Fig. 8, the values of τ_o, estimated using the equation $\tau_o = 1/f_o$, are shown in Table 3. These calculated τ_o values seem to be in the same order of magnitude as those reported by Garcia-Gomes et al. (2010): 3.8–62 s for CM electrodes based on a different precursor [84]. Other studies showed values of τ_o in the range of 3–68 s for carbon electrodes prepared from micro/meso-porous carbon C(Mo_2C) [85]. τ_o values in the range of 0.52–1.37 s for carbon electrodes made from Ginkgo shells were reported by Jiang et al. (2013) [86]. τ_o values of 1 s were reported by Huang et al. (2012) for partially graphitic nanostructures made of porous carbon [87].

3.6.2. Cyclic voltammetry

The supercapacitive performances of the ACMs cells were analyzed using voltammograms recorded at room temperature over the potential range from 0 to 1 V and a scan rate of 1–100 mV s^{-1} Fig. 9(a) shows the measured cyclic voltammograms

Table 4
Specific capacitance values from the EIS, CV and GCD methods for all cells.

Cell	C_{sp} (F g^{-1})		
	EIS	CV	GCD
ACM-0	91	121	118
ACM-5	137	196	186
ACM-15	17.58	11.02	3.38
ACM-20	1.94	11.70	4.66
Ref. [92]	175–376	–	60–287
Ref. [93]	–	78–99	68–245
Ref. [94]	158	–	–
Ref. [95]	–	–	61–104
Ref. [96]	–	47–122	–

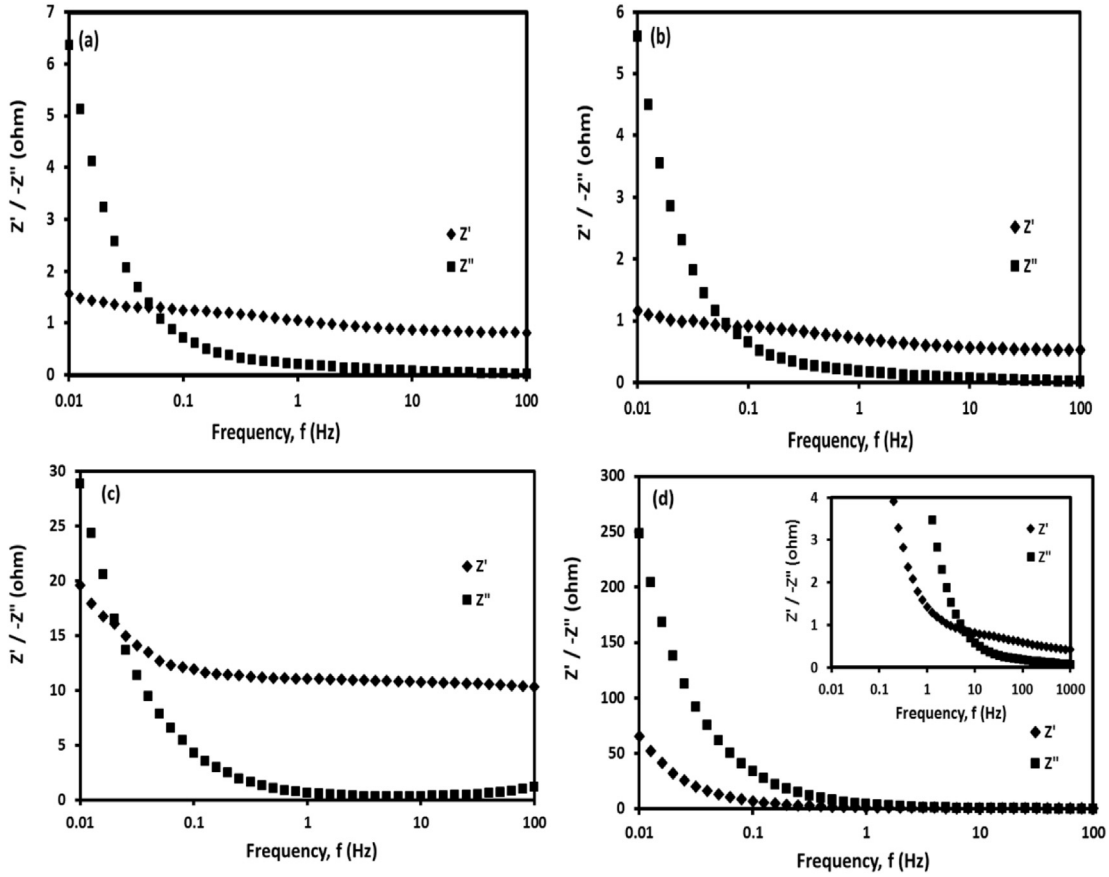

Fig. 8. Bode plot for all cells (a) ACM-0, (b) ACM-5, (c) ACM-15 and (d) ACM-20.

recorded at 1 mV s^{-1} for the ACMs cells. The voltammograms are nearly rectangular for all of the cells, which is a typical for electric double-layer capacitance [88]. Comparisons between the voltammograms in Fig. 9(a) show that the ACM-5 cell has a broader voltammogram area. These results indicate that the ACM-5 cell exhibits a better cycle reversibility and higher electric double-layer capacitance stability during the charge and discharge processes compared with the other cells, as revealed by its higher C_{sp} value. The C_{sp} of ACMs cells calculated using equation (5) from the voltammograms (Fig. 9(a)) are shown in Table 4, and these results are in good agreement with the EIS results.

It can also be observed that the voltammograms in Fig. 9(a) do not have any peaks, indicating that the supercapacitive behavior is free from redox reactions or is purely based on an electrostatic mechanism. Similar features were observed in all of the voltammograms when the scan rate was performed at five different scan rates (1, 5, 25, 50, and 100 mV s^{-1}), as shown in Fig. 10. This figure shows that the current response increased with the scan rate. When the scan rate was greater than 5 mV s^{-1}, the voltammogram 'window' tilted toward the vertical axis and turn into a quasi-rectangle shape. This result indicates that, at lower scan rates, double layer formation dominates the energy storage process.

Fig. 9(b) shows the C_{sp} values at different scan rates for all the ACM cells determined from the voltammogram in Fig. 9(a) using equation (5). All cells exhibit a similar decreasing trend in the C_{sp} values with increasing scan rate. At very low scan rates, the C_{sp}

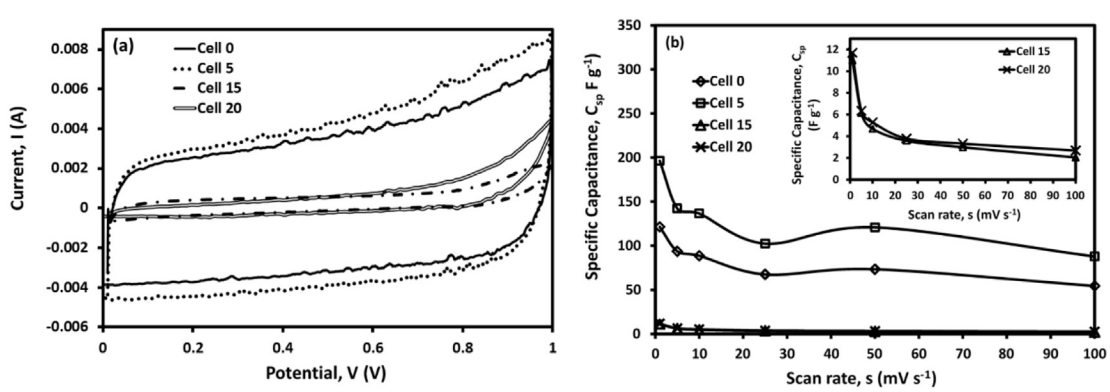

ecific capacitances at different scan rates for all of the cells.

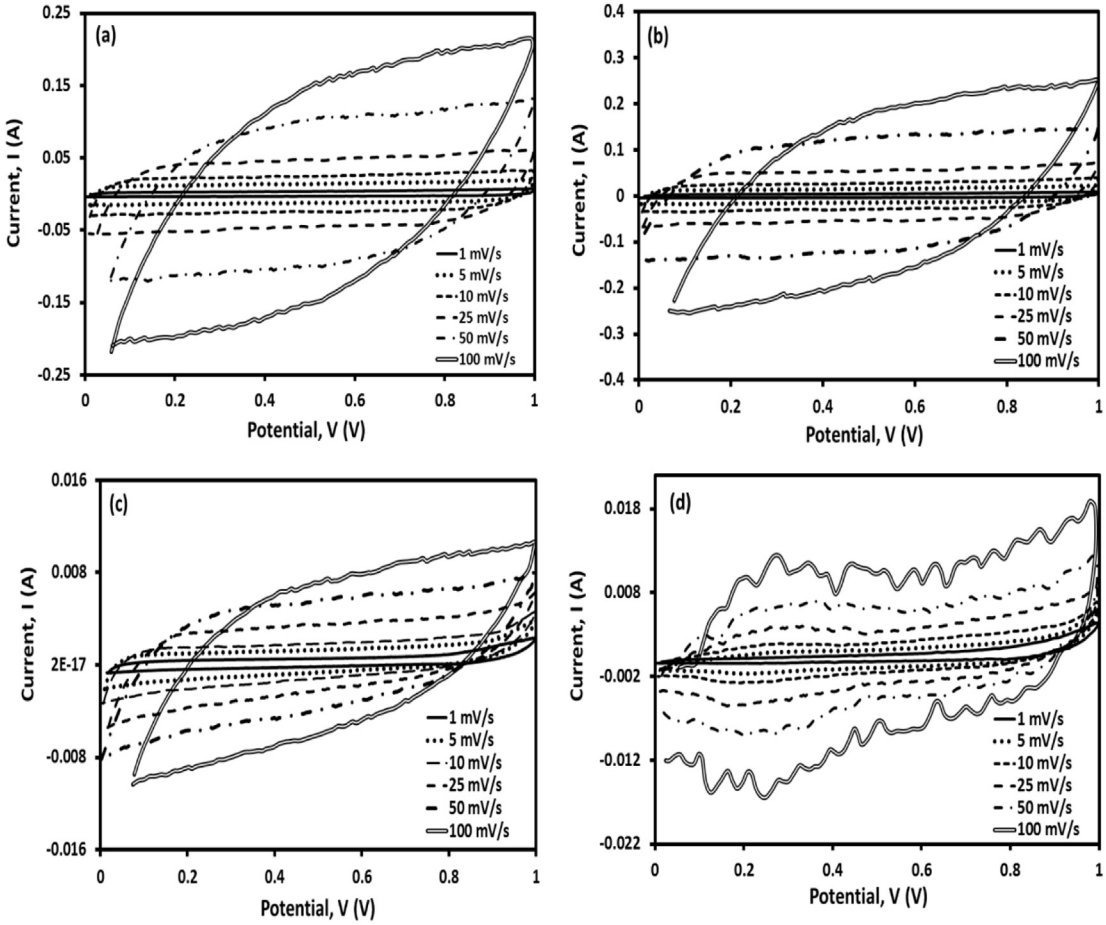

Fig. 10. Voltammograms for 1–100 mV s^{-1} for all cells, (a) ACM-0, (b) ACM-5, (c) ACM-15 and (d) ACM-20.

values are known to be higher because the ions have more time to penetrate and reside in all the available electrode pores and form electric double layers, which are needed to generate higher capacitances. The ACM-5 cell shows higher C_{sp} values over the entire scan region, indicating its superiority over the other three cells. This result agrees well with the EIS results discussed in the previous section. For the scan rate region above 10 mV s^{-1}, the C_{sp} for all of the cells continue to decrease and become very small as the scan rate increases due to the increasing diffusion resistance towards the ionic motion into the electrode pores. This resistance seems to be non-linear with respect to the change in dosage. This non-linear effect was also observed in the dependency of the electrode C_{sp} values on the quantity of binder used during the electrode preparation [89].

3.6.3. Galvanostatic charge–discharge

The GCD curves for all the ACMs cells recorded over the potential range of 0–1 V at a current density of 10 mA cm^{-2} are shown in Fig. 11(a). It was found that all of the cells show a similar symmetrical triangular curve with a nearly linear variation in the voltage as a function of time during charge and discharge. This shape is typical for carbon-based supercapacitors; however, the data show that the ACM-0 and ACM-5 cells have superior supercapacitive performances compared to the other two cells, particularly the ACM-5 cell, which shows the highest charge and discharge times, as shown in Fig. 11(a). These results indicate that a larger number of electrons and electrolyte ions are involved in the charge

other electrodes. This result is consistent with the EIS and CV results that the optimum dosage can enhance electrode performance, suggesting that insufficient and excessive dosage levels must be avoided during electrode preparation.

A sharp drop in the initial voltage of the discharge curve in Fig. 11(a) was found for all cells, and this drop resulted from the diffusion-limited mobility of the electrolyte ions in the electrode pores. This limitation is associated with the ESR (equivalent series resistance) of the supercapacitor cells, which can be calculated from this voltage drop using the equation ESR = $iR_{drop}/2i$. The calculated ESR values for the ACM-0, ACM-5, ACM-15 and ACM-20 cells were 1.247, 0.898, 16.648 and 9.784 Ω, respectively, indicating a strong dependency of the ESR on the dosage. These ESR values are comparable with the other reported ESR values, which range from 9.7 to 16.7 Ω for carbon electrodes derived from activated carbon powder [90] and 1.17–3.69 Ω for carbon electrode mixtures composed of activated carbon, graphite and PTFE (polytetrafluoroethylene) [91] and also with the values listed in Table 5. Reports that ESR values derived from GCD data are higher than those derived from the EIS data are commonly found in the literature. Additionally, our results seem to exhibit a similar trend.

The C_{sp} values of the ACMs cells were calculated from the data in Fig. 11(a) using equation (6) and are shown in Table 4. As expected, these values support the trend in the C_{sp} values calculated from the EIS and CV data, i.e., an overall similar dependence of the C_{sp} on dosage. For comparison, Table 4 lists some of the C_{sp} values reported in the literature for other types of carbon electrodes used in supercapacitors [92–96].

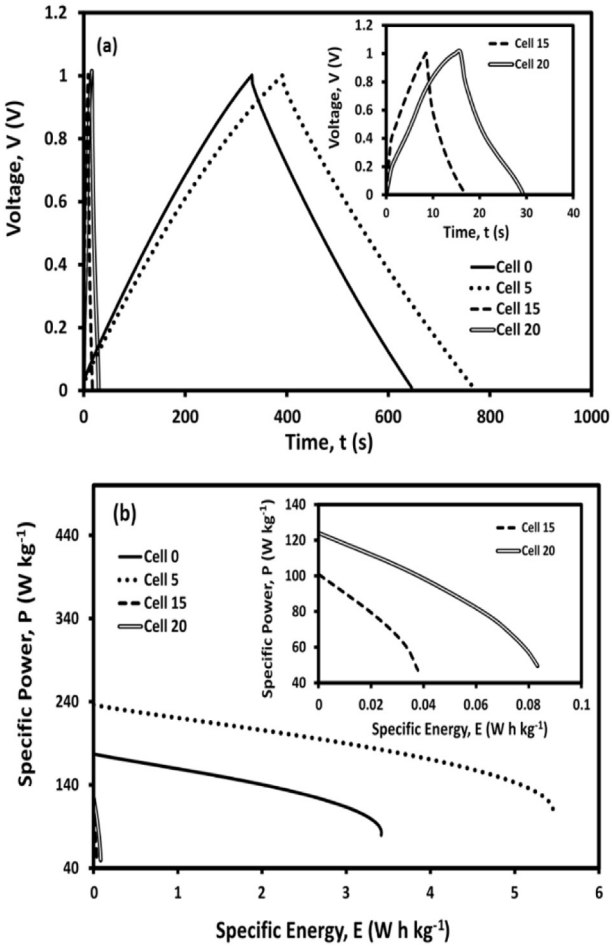

Fig. 11. (a) GCD curves and (b) Ragone plot for all ACMs cells.

3.6.4. Specific energy and power

The specific power and specific energy of the ACM cells were calculated from the GCD curves in Fig. 11(a) using equations (7) and (8), respectively [97]. The results are shown as Ragone plots in Fig. 11(b), representing a correlation between the specific power and specific energy of the supercapacitor.

The specific power linearly decreases with increasing specific energy for all of the cells; less energy is released at higher power outputs. However, a strong influence of the dosage can be observed in Fig. 11(b), the power–energy relationships for the ACM-0 and ACM-5 cells are much better than those of the other two cells, demonstrating that an optimum dosage may improve the performance of the ACM electrodes for supercapacitor application (as shown by the EIS and CV data in the preceding sections). The maximum specific energy and specific power determined for all cells are shown in Table 5. As can be seen in this table, these results are comparable to the typical ranges of specific energy and specific power values reported for supercapacitor electrodes prepared from other types of biomass precursors, i.e., walnut shells [36], rubberwood sawdust [52], cherry stones [97], oil palm empty fruit bunch fibers [53,83,98–100], sunflower seed shells [101], sugarcane bagasse [102], pistachio nutshell [103], birch wood [104], hemp bast fiber [105] and bamboo [106].

It is interesting to examine further the E_{max} and P_{max} values in Table 5. It is convenient to observe the plot of P_{max} value arranged in ascending order against their corresponding E_{max} values as shown in Fig. 12(a) and (b) for supercapacitor using aqueous and organic electrolytes respectively. Fig. 12(a) shows that the trend of P_{max} or E_{max} values obtained by independent effort of those researchers do not establish an 'ideal' desired trend that the effort to increase the P_{max} values must be followed by the increase in the E_{max} values. This figure shows there has been one order of magnitude increase in P_{max}. However, there has not been similar increase in the E_{max}. Fig. 12(b) shows that the energy data for the organics electrolyte is expectedly significantly higher than that of the aqueous electrolyte because of its higher working potential, but the data still exhibit the same trend as observed in Fig. 12(a). Moreover the P_{max} values has reached a plateau. Without fulfilling such an ideal trend, the goal to bring the energy density capability of the supercapacitor with higher power density closer to that of the battery could not be achieved. This analysis seems to suggest that developing carbon based supercapacitor with the approach that employing the electrode-electrolyte materials which can generate capacitance only through non-faradaic process needs reassessment because it does not actually lead to the improved trend in the effort of developing supercapacitor with higher power and energy density. Therefore, it can be noticed in the literature that there have been also concerted effort to exploit both non-faradaic (electrostatic double layer capacitance) and faradaic (pseudocapacitance) processes to generate higher resultant capacitance in developing supercapacitor with higher power and energy density. Their aim is to fully utilize the advantages of the electrostatic capacitance and pseudocapacitance as well as to minimize their relative disadvantages. This is done by fabricating hybrid supercapacitor using different types of the electrode configurations, namely composite, asymmetric and battery-types [107].

Table 5
The values of ESR (GCD), specific power (P), and specific energy (E) for all cells compared to the values reported in other works ([x]Present study, [y]aqueous electrolyte, [z]organic electrolyte).

Precursor	ESR(Ω) (GCD)	[y]P (W kg^{-1})	[y]E (W h kg^{-1})	[z]P (W kg^{-1})	[z]E (W h kg^{-1})
[x]ACM-0	1.247	80–177	0.5×10^{-3}–3.41	–	–
[x]ACM-5	0.898	110–236	0.7×10^{-3}–5.45	–	–
[x]ACM-15	16.648	47–101	0.3×10^{-3}–0.04	–	–
[x]ACM-20	9.784	50–124	3×10^{-3}–0.08	–	–
[36]	0.57	650–1070	4.6–10.2	–	–
[52]	0.018–0.34	275–288	2.5–3.3	–	–
[53]	2.44–4.85	90–161	0.5–2.2	–	–
[83]	0.99–5.94	133–198	0.43–3.82	–	–
[97]	–	700–1200	3.5–5.5	1000–5500	14–18
[98]	1.008–1.645	171–173	3.2–4.3	–	–
[99]	0.26–1.46	159–160	2.4–3.9	–	–
[100]	0.77–1.25	177–179	3.42–4.27	–	–
[101]	–	1400–2400	2.7–4.8	–	–
[102]	–	571–3600	5–7	–	–
[103]	0.01–0.075	52	10	286	39
[104]	–	828–2000	3.5–6.5	2590–7000	20–28
[105]	0.01–0.03	–	–	2800–7700	19–40
[106]	–	2000–2250	2.25–3.45	–	–

4. Conclusions

GMs (Green monoliths) of self-adhesive carbon grains from fibers of oil palm empty fruit bunches and GMs irradiated with 5, 15 and 20 kGy dosages of γ-radiation were carbonized and activated to produce activated carbon monoliths (ACMs) for supercapacitor electrode applications. Low doses (5 kGy) and higher doses (above 5 kGy) induced minor and major changes in the chemical structure of the GMs, respectively, which affected the porosity and network of pores produced in the ACMs during carbonization and activation. A low dosage was found to be optimum for enhancing the performance of supercapacitors and can produce a specific capacitance of

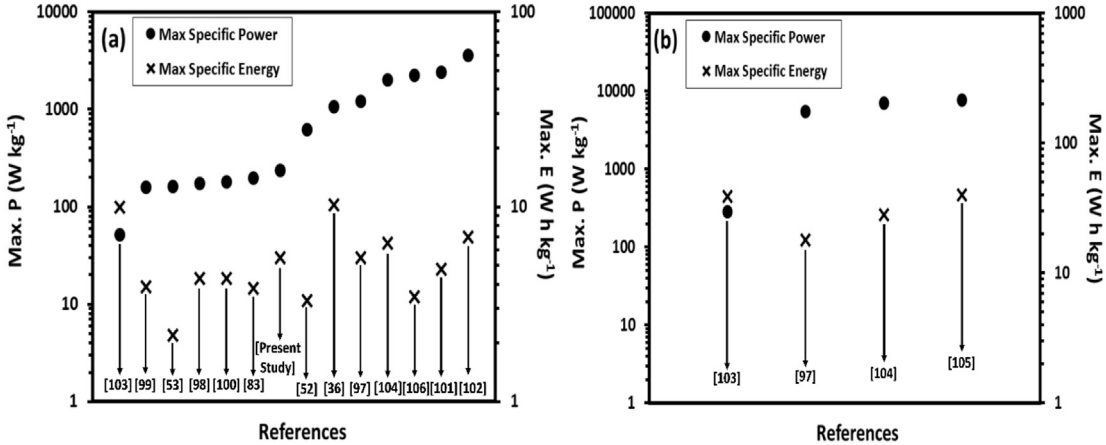

Fig. 12. Maximum specific power and maximum specific energy data from different references using (a) aqueous and (b) organic electrolytes.

196 F g^{-1}, corresponding to a specific power of 236 W kg^{-1} and specific energy of 5.45 W h kg^{-1}, which represent 60%–90%, 30%–50% and 60%–100% percents or greater improvement compared with the values recorded for supercapacitor cells using ACMs from non-irradiated GMs and γ-irradiated GMs at higher dosages. This study contributes to the continuing research and development on using renewable materials such as oil palm empty fruit bunches as precursors to produce electrodes for energy-storage devices. It also promotes the use of the γ-irradiation method, a simple but effective approach useful for modifying the precursor in producing a higher quality electrode for energy storage devices.

Acknowledgments

We acknowledge the grants from the Ministry of High Education (FRGS/2/2013/ST05/UKM/01/1), Ministry of Science, Technology and Innovation (03-01-02-SF1118) and Universiti Kebangsaan Malaysia (DIP-2014-027, UKM-Industri-2013-023) and the support of Centre of Research Innovation and Management. The authors also thank to Mr. Saini for help with the laboratory work.

References

[1] Pasquier A Du, Plitz I, Menocal S, Amatucci G. A comparative study of Li-ion battery, supercapacitor and nonaqueous asymmetric hybrid devices for automotive applications. J Power Sources 2003;115(1):171–8.
[2] Taberna P-L, Chevallier G, Simon P, Plée D, Aubert T. Activated carbon–carbon nanotube composite porous film for supercapacitor applications. Mater Res Bull 2006;41(3):478–84.
[3] Hu X, Murgovski N, Mardh Johannesson L, Egardt B. Comparison of three electrochemical energy buffers applied to a hybrid bus powertrain with simultaneous optimal sizing and energy management. IEEE Trans Intell Transp Syst 2014;15(3):1193–205.
[4] Choi H-J, Jung S-M, Seo J-M, Chang DW, Dai L, Baek J-B. Graphene for energy conversion and storage in fuel cells and supercapacitors. Nano Energy 2012;1(4):534–51.
[5] Wang H, Zhang D, Yan T, Wen X, Zhang J, Shi L, et al. Three-dimensional macroporous graphene architectures as high performance electrodes for capacitive deionization. J Mater Chem A 2013;1(38):11778–89.
[6] Wang H, Zhang D, Yan T, Wen X, Shi L, Zhang J. Graphene prepared via a novel pyridine–thermal strategy for capacitive deionization. J Mater Chem 2012;22(45):23745–8.
[7] Wang H, Shi L, Yan T, Zhang J. Design of graphene-coated hollow mesoporous carbon spheres as high performance electrodes for capacitive deionization. J Mater Chem A 2014;2(13):4739–50.
[8] Pan H, Li J, Feng Y. Carbon nanotubes for supercapacitor. Nanoscale Res Lett 2010;5(3):654–68.
[9] Huang K-J, Wang L, Zhang J-Z, Wang L-L, Mo Y-P. One-step preparation of layered molybdenum disulfide/multi-walled carbon nanotube composites for enhanced performance supercapacitor. Energy 2014;67:234–40.
[10] Ramya R, Sivasubramaniam R, Sangaranarayanan MV. Conducting polymers-based electrochemical supercapacitors-progress and prospects. Electrochim
[11] Kim J, Ju H, Inamdar AI, Jo Y, Han J, Kim H, et al. Synthesis and enhanced electrochemical supercapacitor properties of Ag–MnO_2–polyaniline nanocomposite electrodes. Energy 2014;70:473–7.
[12] Wen X, Zhang D, Shi L, Yan T, Wang H, Zhang J. Three-dimensional hierarchical porous carbon with a bimodal pore arrangement for capacitive deionization. J Mater Chem 2012;22(45):23835.
[13] Lokhande CD, Dubal DP, Joo O-S. Metal oxide thin film based supercapacitors. Curr Appl Phys 2011;11(3):255–70.
[14] Sieben JM, Morallón E, Cazorla-Amorós D. Flexible ruthenium oxide-activated carbon cloth composites prepared by simple electrodeposition methods. Energy 2013;58:519–26.
[15] Dubal DP, Holze R. All-solid-state flexible thin film supercapacitor based on Mn_3O_4 stacked nanosheets with gel electrolyte. Energy 2013;51:407–12.
[16] Jagadale AD, Kumbhar VS, Bulakhe RN, Lokhande CD. Influence of electrodeposition modes on the supercapacitive performance of Co_3O_4 electrodes. Energy 2014;64:234–41.
[17] Li J, Wang X, Huang Q, Gamboa S, Sebastian PJ. Studies on preparation and performances of carbon aerogel electrodes for the application of supercapacitor. J Power Sources 2006;158(1):784–8.
[18] Jang Y, Jo J, Choi Y-M, Kim I, Lee S-H, Kim D, et al. Activated carbon nanocomposite electrodes for high performance supercapacitors. Electrochim Acta 2013;102:240–5.
[19] Peng C, Yan X, Wang R, Lang J, Ou Y, Xue Q. Promising activated carbons derived from waste tea-leaves and their application in high performance supercapacitors electrodes. Electrochim Acta 2013;87:401–8.
[20] Fan Z, Qi D, Xiao Y, Yan J, Wei T. One-step synthesis of biomass-derived porous carbon foam for high performance supercapacitors. Mater Lett 2013;101:29–32.
[21] Seo M-K, Park S-J. Electrochemical characteristics of activated carbon nanofiber electrodes for supercapacitors. Mater Sci Eng B 2009;164(2):106–11.
[22] Zhang D, Wen X, Shi L, Yan T, Zhang J. Enhanced capacitive deionization of graphene/mesoporous carbon composites. Nanoscale 2012;4(17):5440–6.
[23] Zhang D, Yan T, Shi L, Peng Z, Wen X, Zhang J. Enhanced capacitive deionization performance of graphene/carbon nanotube composites. J Mater Chem 2012;22(29):14696–704.
[24] Peng Z, Zhang D, Yan T, Zhang J, Shi L. Three-dimensional micro/mesoporous carbon composites with carbon nanotube networks for capacitive deionization. Appl Surf Sci 2013;282:965–73.
[25] Fang B, Wei YZ, Maruyama K, Kumagai M. High capacity supercapacitors based on modified activated carbon aerogel. J Appl Electrochem 2005;35(3):229–33.
[26] Zhang L, Candelaria SL, Tian J, Li Y, Huang Y, Cao G. Copper nanocrystal modified activated carbon for supercapacitors with enhanced volumetric energy and power density. J Power Sources 2013;236:215–23.
[27] Elmouwahidi A, Zapata-Benabithe Z, Carrasco-Marín F, Moreno-Castilla C. Activated carbons from KOH-activation of argan (Argania spinosa) seed shells as supercapacitor electrodes. Bioresour Technol 2012;111:185–90.
[28] Sahira J, Mandira A, Prasad P, Ram P. Effects of activating agents on the activated carbons prepared from Lapsi seed stone. Res J Chem Sci 2013;3(5):19–24.
[29] Yakout SM. Multi-component adsorption of benzene, toluene, ethylbenzene and xylenes from aqueous by activated carbon from rice husk. Asian J Chem 2014;26:2809–12.
[30] Adinata D, Wan Daud WMA, Aroua MK. Preparation and characterization of activated carbon from palm shell by chemical activation with K_2CO_3. Bioresour Technol 2007;98(1):145–9.
[31] Molina-Sabio M, Rodrıguez-Reinoso F. Role of chemical activation in the development of carbon porosity. Colloids Surfaces A Physicochem Eng Asp 2004;241(1–3):15–25.

[32] Kumagai S, Sato M, Tashima D. Electrical double-layer capacitance of micro- and mesoporous activated carbon prepared from rice husk and beet sugar. Electrochim Acta 2013;114:617–26.
[33] Rodriguez-Reinoso F, Molina-Sabio M, González M. The use of steam and CO_2 as activating agents in the preparation of activated carbons. Carbon 1995;33(1):15–23.
[34] Petrova B, Tsyntsarski B, Budinova T, Petrov N, Ania CO, Parra JB, et al. Synthesis of nanoporous carbons from mixtures of coal tar pitch and furfural and their application as electrode materials. Fuel Process Technol 2010;91(11):1710–6.
[35] Liu Y, Li J, Lai Y, Song H, Zhang Z. Preparation and properties of pitch carbon based supercapacitor. J Cent South Univ 2007;5:601–6.
[36] Yang J, Liu Y, Chen X, Hu Z, Zhao G. Carbon electrode material with high densities of energy and power. Acta Physico-Chimica Sin 2008;24(1):13–9.
[37] Hu Z, Srinivasan M. Mesoporous high-surface-area activated carbon. Microporous Mesoporous Mater 2001;43(3):267–75.
[38] He X, Ling P, Yu M, Wang X, Zhang X, Zheng M. Rice husk-derived porous carbons with high capacitance by $ZnCl_2$ activation for supercapacitors. Electrochim Acta 2013;105:635–41.
[39] Syarif N, Tribidasari AI, Wibowo W. Direct synthesis carbon/Metal oxide composites for electrochemical capacitors electrode. Trans J Eng Manag Appl Sci Technol 2011;3(1):21–34.
[40] Palanichamy K, Ariharaputhiran A, Darchen A. Activated carbon from grass-A green alternative catalyst support for water electrolysis. Int J Hydrogen Energy 2013;25:10364–72.
[41] Deraman M, Saad SKM, Ishak MM, Taer E, Talib I, Omar R, et al. Carbon/-carbon nanotubes (CNTs) composites from green pellets contain CNTs and self-adhesive carbon grains from fibres of oil palm empty fruit bunch. AIP Conf Proc 2010;1284:179–86.
[42] Deng L, Young RJ, Kinloch I a, Abdelkader AM, Holmes SM, De Haro-Del Rio D a, et al. Supercapacitance from cellulose and carbon nanotube nanocomposite fibers. ACS Appl Mater Interfaces 2013;5(20):9983–90.
[43] Zheng C, Zhou X, Cao H, Wang G, Liu Z. Synthesis of porous graphene/activated carbon composite with high packing density and large specific surface area for supercapacitor electrode material. J Power Sources 2014;258:290–6.
[44] Zhang L, Zhang F, Yang X, Long G, Wu Y, Zhang T, et al. Porous 3D graphene-based bulk materials with exceptional high surface area and excellent conductivity for supercapacitors. Sci Rep 2013;3:1–9.
[45] Awitdrus, Deraman M, Abu Talib I, Omar R, Jumali MHH, Taer E, Mohd Saman M. Dimension and total active surface area of carbon electrode from mixtures of pre-carbonized oil palm empty fruit bunches and green petroleum cokes. Sains Malays 2010;39(1):83–6.
[46] Raymundo-Pinero E, Cazorla-Amoros D, Linares-Solano A, Find J, Wild U, Schlogl R. Structural characterization of N-containing activated carbon fibers prepared from a low softening point petroleum pitch and a melamine resin. Carbon 2002;40:597–608.
[47] Sánchez Orozco R, Balderas Hernández P, Flores Ramírez N, Roa Morales G, Saucedo Luna J, Castro Montoya AJ. Gamma irradiation induced degradation of orange peels. Energies 2012;5(12):3051–63.
[48] Kasprzyk H, Wichlacz K, Borysiak S. The effect of gamma radiation on the supramolecular structure of pine wood cellulose in situ revealed by X-Ray diffraction. Electron J Pol Agric Univ 2004;7(1):1–9.
[49] Takacs E, Wojnarovits L, Borsa J, Foldvary C, Hargittai P, Zold O. Effect of γ-irradiation on cotton-cellulose. Radiat Phys Chem 1999;55:663–6.
[50] Deraman M, Omar R, Harun AG. Young ' s modulus of carbon from self-adhesive carbon grain of oil palm bunches. J Mater Sci Lett 1998;17:2059–60.
[51] Deraman M, Omar R, Zakaria S. Electrical and mechanical properties of carbon pellets from acid (HNO_3) treated self-adhesive carbon grain from oil palm empty fruit bunch. J Mater Sci 2002;37:3329–35.
[52] Taer E, Deraman M, Talib I a, Hashmi S a, Umar A a. Growth of platinum nanoparticles on stainless steel 316L current collectors to improve carbon-based supercapacitor performance. Electrochim Acta 2011;56(27):10217–22.
[53] Farma R, Deraman M, Awitdrus, Talib IA, Omar R, Manjunatha JG, et al. Physical and electrochemical properties of supercapacitor electrodes derived from carbon nanotube and biomass carbon. Int J Electrochem Sci 2013;8:257–73.
[54] Portet C, Taberna PL, Simon P, Flahaut E, Laberty-Robert C. High power density electrodes for carbon supercapacitor applications. Electrochim Acta 2005;50(20):4174–81.
[55] Beidaghi M, Chen W, Wang C. Electrochemically activated carbon micro-electrode arrays for electrochemical micro-capacitors. J Power Sources 2011;196(4):2403–9.
[56] Tsay K-C, Zhang L, Zhang J. Effects of electrode layer composition/thickness and electrolyte concentration on both specific capacitance and energy density of supercapacitor. Electrochim Acta 2012;60:428–36.
[57] Fuertes a B, Lota G, Centeno T a, Frackowiak E. Templated mesoporous carbons for supercapacitor application. Electrochim Acta 2005;50(14):2799–805.
[58] Prabaharan SRS, Vimala R, Zainal Z. Nanostructured mesoporous carbon as electrodes for supercapacitors. J Power Sources 2006;161(1):730–6.
[59] Isroi, Ishola MM, Millati R, Syamsiah S, Cahyanto MN, Niklasson C, et al. Structural changes of oil palm empty fruit bunch (OPEFB) after fungal and phosphoric acid pretreatment. Molecules 2012;17(12):14995–5012.
[60] Nazir M, Wahjoedi B, Yussof A, Abdullah M. Eco-friendly extraction and characterization of cellulose from oil palm empty fruit bunches. BioResources 2013;8(2):2161–72.
[61] El-Hendawy A-N a. Variation in the FTIR spectra of a biomass under impregnation, carbonization and oxidation conditions. J Anal Appl Pyrol 2006;75(2):159–66.
[62] Khan F, Ahmad SR, Kronfli E. Gamma-radiation induced changes in the physical and chemical properties of lignocellulose. Biomacromolecules 2006;7(8):2303–9.
[63] Moshiul Alam AKM, Beg MDH, Reddy Prasad DM, Khan MR, Mina MF. Structures and performances of simultaneous ultrasound and alkali treated oil palm empty fruit bunch fiber reinforced poly(lactic acid) composites. Compos Part A Appl Sci Manuf 2012;43(11):1921–9.
[64] Amin N, Misson M, Haron R. Bio-oils and diesel fuel derived from alkaline treated empty fruit bunch (EFB). Int J Biomass Renew 2012;1:6–14.
[65] Wahi R, Ngaini Z, Jok V. Removal of mercury, lead and copper from aqueous solution by activated carbon of palm oil empty fruit bunch. World Appl Sci J 2009;5:84–91.
[66] Pua FL, Zakaria S, Chia CH, Fan SP, Rosenau T, Potthast A, et al. Solvolytic liquefaction of oil palm empty fruit bunch (EFB) fibres: analysis of product fractions using FTIR and pyrolysis-GCMS. Sains Malays 2013;42(6):793–9.
[67] Coutinho a, Rocha J, Luengo C. Preparing and characterizing biocarbon electrodes. Fuel Process Technol 2000;67(2):93–102.
[68] Deraman M, Zakaria S, Murshidi JA. Estimation of crystallinity and crystallite size of cellulose in benzylated fibres of oil palm empty fruit bunches by X-ray diffraction. Jpn J Appl Phys 2001;40:3311–4.
[69] Nabais JMV, Teixeira JG, Almeida I. Development of easy made low cost bindless monolithic electrodes from biomass with controlled properties to be used as electrochemical capacitors. Bioresour Technol 2011;102(3):2781–7.
[70] Khalil HPSA, Jawaid M, Firoozian P, Rashid U, Islam A, Akil HM. Activated carbon from various Agricultural wastes by chemical activation with KOH: preparation and characterization. J Biobased Mater Bioenergy 2013;7(6):708–14.
[71] Hamad BK, Noor AM, Rahim AA. Removal of 4-chloro-2-methoxyphenol from aqueous solution by adsorption to oil palm shell activated carbon activated with K_2CO_3. J Phys Sci 2011;22(1):39–55.
[72] Sing KSW, Everett DH, Haul RAW, Moscou L, Pierotti RA, Rouquerol J, et al. Reporting physisorption data for gas/solid systems with special reference to the determination of surface area and porosity. Pure Appl Chem 1985;57(4):603–19.
[73] Chen H, Wang F, Tong S, Guo S, Pan X. Porous carbon with tailored pore size for electric double layer capacitors application. Appl Surf Sci 2012;258(16):6097–102.
[74] Chen Y, Zhang X, Zhang H, Sun X, Zhang D, Ma Y. High-performance supercapacitors based on a graphene–activated carbon composite prepared by chemical activation. RSC Adv 2012;2(20):7747.
[75] Wen X, Zhang D, Yan T, Zhang J, Shi L. Three-dimensional graphene-based hierarchically porous carbon composites prepared by a dual-template strategy for capacitive deionization. J Mater Chem A 2013;1(39):12334.
[76] Kim Y-J, Lee B-J, Suezaki H, Chino T, Abe Y, Yanagiura T, et al. Preparation and characterization of bamboo-based activated carbons as electrode materials for electric double layer capacitors. Carbon 2006;44(8):1592–5.
[77] Du S-H, Wang L-Q, Fu X-T, Chen M-M, Wang C-Y. Hierarchical porous carbon microspheres derived from porous starch for use in high-rate electrochemical double-layer capacitors. Bioresour Technol 2013;139:406–9.
[78] Raymundo-Piñero E, Cadek M, Wachtler M, Béguin F. Carbon nanotubes as nanotexturing agents for high power supercapacitors based on seaweed carbons. ChemSusChem 2011;4(7):943–9.
[79] Chen W-C, Wen T-C, Teng H. Polyaniline-deposited porous carbon electrode for supercapacitor. Electrochim Acta 2003;48(6):641–9.
[80] Rafik F, Gualous H, Gallay R, Crausaz A, Berthon A. Frequency, thermal and voltage supercapacitor characterization and modeling. J Power Sources 2007;165(2):928–34.
[81] Nian Y, Teng H. Influence of surface oxides on the impedance behavior of carbon-based electrochemical capacitors. J Electroanal Chem 2003;540:119–27.
[82] Gamby J, Taberna P, Simon P, Fauvarque J, Chesneau M. Studies and characterisations of various activated carbons used for carbon/carbon supercapacitors. J Power Sources 2001;101(1):109–16.
[83] Basri NH, Deraman M, Kanwal S, Talib I a, Manjunatha JG, Aziz A a, et al. Supercapacitors using binderless composite monolith electrodes from carbon nanotubes and pre-carbonized biomass residues. Biomass Bioenerg 2013;59:370–9.
[84] Garcia-Gomez a, Miles P, Centeno T a, Rojo JM. Uniaxially oriented carbon monoliths as supercapacitor electrodes. Electrochim Acta 2010;55(28):8539–44.
[85] Thomberg T, Jänes A, Lust E. Energy and power performance of electrochemical double-layer capacitors based on molybdenum carbide derived carbon. Electrochim Acta 2010;55(9):3138–43.
[86] Jiang L, Yan J, Hao L, Sun G. High rate performance activated carbons prepared from ginkgo shells for electrochemical supercapacitors. Carbon 2013;56:146–54.
[87] Huang C-H, Zhang Q, Chou T-C, Chen C-M, Su DS, Doong R-A. Three-dimensional hierarchically ordered porous carbons with partially graphitic

nanostructures for electrochemical capacitive energy storage. ChemSusChem 2012;5(3):563–71.
[88] Inamdar a I, Kim Y, Pawar SM, Kim JH, Im H, Kim H. Chemically grown, porous, nickel oxide thin-film for electrochemical supercapacitors. J Power Sources 2011;196(4):2393–7.
[89] Yan J, Wei T, Shao B, Fan Z, Qian W, Zhang M, et al. Preparation of a graphene nanosheet/polyaniline composite with high specific capacitance. Carbon 2010;48(2):487–93.
[90] Kim K-M, Hur J-W, Jung S-I, Kang A-S. Electrochemical characteristics of activated carbon/Ppy electrode combined with P(VdF-co-HFP)/PVP for EDLC. Electrochim Acta 2004;50(2–3):863–72.
[91] Yu H, Wu J, Fan L, Xu K, Zhong X, Lin Y, et al. Improvement of the performance for quasi-solid-state supercapacitor by using PVA–KOH–KI polymer gel electrolyte. Electrochim Acta 2011;56(20):6881–6.
[92] Du X, Zhao W, Wang Y, Wang C, Chen M, Qi T, et al. Preparation of activated carbon hollow fibers from ramie at low temperature for electric double-layer capacitor applications. Bioresour Technol 2013;149:31–7.
[93] He X, Ling P, Qiu J, Yu M, Zhang X, Yu C, et al. Efficient preparation of biomass-based mesoporous carbons for supercapacitors with both high energy density and high power density. J Power Sources 2013;240:109–13.
[94] Boukmouche N, Azzouz N, Bouchama L, Chopart JP, Bouznit Y. Activated carbon derived from marine posidonia oceanica for electric energy storage. Arab J Chem 2014;7:347–54.
[95] Ong LK, Kurniawan A, Suwandi AC, Lin CX, Zhao XS, Ismadji S. A facile and green preparation of durian shell-derived carbon electrodes for electrochemical double-layer capacitors. Prog Nat Sci 2012;22(6):624–30.
[96] Hu C-C, Wang C-C, Wu F-C, Tseng R-L. Characterization of pistachio shell-derived carbons activated by a combination of KOH and CO_2 for electric double-layer capacitors. Electrochim Acta 2007;52(7):2498–505.
[97] Olivares-Marín M, Fernández J a, Lázaro MJ, Fernández-González C, Macías-García A, Gómez-Serrano V, et al. Cherry stones as precursor of activated carbons for supercapacitors. Mater Chem Phys 2009;114(1):323–7.
[98] Farma R, Deraman M, Awitdrus A, Talib I a, Taer E, Basri NH, et al. Preparation of highly porous binderless activated carbon electrodes from fibres of oil palm empty fruit bunches for application in supercapacitors. Bioresour Technol 2013;132:254–61.
[99] Dolah BNM, Deraman M, Othman MAR, Farma R, Taer E, Basri NH, et al. A method to produce binderless supercapacitor electrode monoliths from biomass carbon and carbon nanotubes. Mater Res Bull 2014;60:10–9.
[100] Nor NSM, Deraman M, Omar R, Taer E, Farma R, Basri NH, et al. Nanoporous separators for supercapacitor using activated carbon monolith electrode from oil palm empty fruit bunches. AIP Conf Proc 2014;1586:68–73.
[101] Li X, Xing W, Zhuo S, Zhou J, Li F, Qiao S-Z, et al. Preparation of capacitor's electrode from sunflower seed shell. Bioresour Technol 2011;102(2):1118–23.
[102] Wahid M, Puthusseri D, Phase D, Ogale S. Enhanced capacitance retention in a supercapacitor made of carbon from sugarcane bagasse by hydrothermal pretreatment. Energy Fuels 2014;28(6):4233–40.
[103] Xu J, Gao Q, Zhang Y, Tan Y, Tian W, Zhu L, et al. Preparing two-dimensional microporous carbon from Pistachio nutshell with high areal capacitance as supercapacitor materials. Sci Rep 2014;4:5545–50.
[104] Dobele G, Dizhbite T, Gil MV, Volperts A, Centeno T a. Production of nanoporous carbons from wood processing wastes and their use in supercapacitors and CO_2 capture. Biomass Bioenerg 2012;46:145–54.
[105] Wang H, Xu Z, Kohandehghan A, Li Z, Cui K, Tan X, et al. Interconnected carbon nanosheets derived from hemp for ultrafast supercapacitors with high energy. ACS Nano 2013;7(6):5131–41.
[106] Yang C-S, Jang YS, Jeong HK. Bamboo-based activated carbon for supercapacitor applications. Curr Appl Phys 2014;14(12):1616–20.
[107] Staaf LGH, Lundgren P, Enoksson P. Present and future supercapacitor carbon electrode materials for improved energy storage used in intelligent wireless sensor systems. Nano Energy 2014;9:128–41.